Modeling photovoltaic performance in periodic patterned colloidal quantum dot solar cells

Yulan Fu,[1] Abay G. Dinku,[2] Yukihiro Hara,[1] Christopher W. Miller,[1] Kristina T. Vrouwenvelder,[1] and Rene Lopez[1,*]

[1] *Department of Physics and Astronomy, University of North Carolina at Chapel Hill, Phillips Hall, CB 3255, Chapel Hill, NC 27599, USA*
[2] *Department of Chemistry, University of North Carolina at Chapel Hill, Caudill and Kenan Laboratories, CB 3290 Chapel Hill, NC 27599, USA*
*rln@physics.unc.edu

Abstract: Colloidal quantum dot (CQD) solar cells have attracted tremendous attention mostly due to their wide absorption spectrum window and potentially low processability cost. The ultimate efficiency of CQD solar cells is highly limited by their high trap state density. Here we show that the overall device power conversion efficiency could be improved by employing photonic structures that enhance both charge generation and collection efficiencies. By employing a two-dimensional numerical model, we have calculated the characteristics of patterned CQD solar cells based of a simple grating structure. Our calculation predicts a power conversion efficiency as high as 11.2%, with a short circuit current density of 35.2 mA/cm^2, a value nearly 1.5 times larger than the conventional flat design, showing the great potential value of patterned quantum dot solar cells.

OCIS codes: (310.4165) Multilayer design; (310.6628) Subwavelength structures, nanostructures; (310.6845) Thin film devices and applications; (350.6050) Solar energy; (040.5350) Photovoltaic.

References and links

1. J. Y. Kim, O. Voznyy, D. Zhitomirsky, and E. H. Sargent, "25th anniversary article: Colloidal quantum dot materials and devices: A quarter-century of advances," Adv. Mater. **25**(36), 4986–5010 (2013).
2. M. G. Bawendi, M. L. Steigerwald, and L. E. Brus, "The quantum mechanics of larger semiconductorclusters ("quantum dots")," Annu. Rev. Phys. Chem. **41**(1), 477–496 (1990).
3. A. P. Alivisatos, A. L. Harris, N. J. Levinos, M. L. Steigerwald, and L. E. Brus, "Electronic states of semiconductor clusters: Homogeneous and inhomogeneous broadening of the optical spectrum," J. Chem. Phys. **89**(7), 4001–4011 (1988).
4. P. Maraghechi, A. J. Labelle, A. R. Kirmani, X. Lan, M. M. Adachi, S. M. Thon, S. Hoogland, A. Lee, Z. Ning, A. Fischer, A. Amassian, and E. H. Sargent, "The donor-supply electrode enhances performance in colloidal quantum dot solar cells," ACS Nano **7**(7), 6111–6116 (2013).
5. A. G. Pattantyus-Abraham, I. J. Kramer, A. R. Barkhouse, X. Wang, G. Konstantatos, R. Debnath, L. Levina, I. Raabe, M. K. Nazeeruddin, M. Grätzel, and E. H. Sargent, "Depleted-heterojunction colloidal quantum dot solar cells," ACS Nano **4**(6), 3374–3380 (2010).
6. Z. Ning, D. Zhitomirsky, V. Adinolfi, B. Sutherland, J. Xu, O. Voznyy, P. Maraghechi, X. Lan, S. Hoogland, Y. Ren, and E. H. Sargent, "Graded doping for enhanced colloidal quantum dot photovoltaics," Adv. Mater. **25**(12), 1719–1723 (2013).
7. C.-H. M. Chuang, P. R. Brown, V. Bulović, and M. G. Bawendi, "Improved performance and stability in quantum dot solar cells through band alignment engineering," Nat. Mater. **13**(8), 796–801 (2014).
8. A. H. Ip, S. M. Thon, S. Hoogland, O. Voznyy, D. Zhitomirsky, R. Debnath, L. Levina, L. R. Rollny, G. H. Carey, A. Fischer, K. W. Kemp, I. J. Kramer, Z. Ning, A. J. Labelle, K. W. Chou, A. Amassian, and E. H. Sargent, "Hybrid passivated colloidal quantum dot solids," Nat. Nanotechnol. **7**(9), 577–582 (2012).
9. D. Zhitomirsky, O. Voznyy, L. Levina, S. Hoogland, K. W. Kemp, A. H. Ip, S. M. Thon, and E. H. Sargent, "Engineering colloidal quantum dot solids within and beyond the mobility-invariant regime," Nat. Commun. **5**, 3803 (2014).
10. K. S. Jeong, J. Tang, H. Liu, J. Kim, A. W. Schaefer, K. Kemp, L. Levina, X. Wang, S. Hoogland, R. Debnath, L. Brzozowski, E. H. Sargent, and J. B. Asbury, "Enhanced mobility-lifetime products in PbS colloidal quantum dot photovoltaics," ACS Nano **6**(1), 89–99 (2012).
11. G. I. Koleilat, L. Levina, H. Shukla, S. H. Myrskog, S. Hinds, A. G. Pattantyus-Abraham, and E. H. Sargent, "Efficient, stable infrared photovoltaics based on solution-cast colloidal quantum dots," ACS Nano **2**(5), 833–840 (2008).

12. W. Fawcett, A. D. Boardman, and S. Swain, "Monte Carlo determination of electron transport properties in gallium arsenide," J. Phys. Chem. Solids **31**(9), 1963–1990 (1970).
13. S. Bandyopadhyay, M. E. Klausmeier-Brown, C. M. Maziar, S. Datta, and M. S. Lundstrom, "A rigorous technique to couple Monte Carlo and drift-diffusion models for computationally efficient device simulation," IEEE Trans. Electron. Dev. **34**(2), 392–399 (1987).
14. R. Stewart, L. Ye, and J. Churchill, "Improved relaxation-time formulation of collision terms for two-band hydrodynamic models," Solid-State Electron. **32**(6), 497–502 (1989).
15. M. S. Lundstrom and R. J. Schuelke, "Numerical analysis of heterostructure semiconductor devices," IEEE Trans. Electron. Dev. **30**(9), 1151–1159 (1983).
16. K. Yang, J. R. East, and G. I. Haddad, "Numerical modeling of abrupt heterojunctions using a thermionic-field emission boundary condition," Solid-State Electron. **36**(3), 321–330 (1993).
17. M. M. Adachi, A. J. Labelle, S. M. Thon, X. Lan, S. Hoogland, and E. H. Sargent, "Broadband solar absorption enhancement via periodic nanostructuring of electrodes," Sci. Rep. **3**, 2928 (2013).
18. D. A. R. Barkhouse, O. Gunawan, T. Gokmen, T. K. Todorov, and D. B. Mitzi, "Device characteristics of a 10.1% hydrazine-processed Cu$_2$ZnSn(Se,S)$_4$ solar cell," Prog. Photovolt. Res. Appl. **20**(1), 6–11 (2012).
19. J. Tang, H. Liu, D. Zhitomirsky, S. Hoogland, X. Wang, M. Furukawa, L. Levina, and E. H. Sargent, "Quantum junction solar cells," Nano Lett. **12**(9), 4889–4894 (2012).
20. A. Descoeudres, Z. C. Holman, L. Barraud, S. Morel, S. De Wolf, and C. Ballif, ">21% Efficient silicon heterojunction solar cells on n- and p-type wafers compared," IEEE J. Photovoltaics **3**(1), 83–89 (2013).
21. W. Wang, M. T. Winkler, O. Gunawan, T. Gokmen, T. K. Todorov, Y. Zhu, and D. B. Mitzi, "Device characteristics of CZTSSe thin-film solar cells with 12.6% efficiency," Adv. Energy Mater. **4**(7), 1301465 (2014).
22. Y. Liu, C. Kirsch, A. Gadisa, M. Aryal, S. Mitran, E. T. Samulski, and R. Lopez, "Effects of nano-patterned versus simple flat active layers in upright organic photovoltaic devices," J. Phys. D Appl. Phys. **46**(2), 024008 (2013).
23. A. J. Labelle, S. M. Thon, S. Masala, M. M. Adachi, H. Dong, M. Farahani, A. H. Ip, A. Fratalocchi, and E. H. Sargent, "Colloidal quantum dot solar cells exploiting hierarchical structuring," Nano Lett. **15**(2), 1101–1108 (2015).

1. Introduction

Semiconducting colloidal quantum dots (CQDs) such as PbS have attracted great interest in recent years for applications in optoelectronic devices, particularly photovoltaic solar cells. This is because their tunable band gap allows wide visible and infrared light absorption, and their potential low cost due to their excellent solution-processability [1–3]. These devices typically exhibit an infrared spectral response well beyond that of other solution processed materials. As 50% of the sun's energy lies beyond $\lambda = 800$ nm, capturing deep infrared photons is a key feature that CQDs can provide. CQD device operation typically utilizes a charge depletion region formed within the p-type CQD layer to separate photo-generated electron-hole pairs through an interface formed when the p-type CQD is in contact with a suitable n-type semiconductor. PbS CQD devices having heterojunctions with low-cost n-type oxides such as TiO$_2$ can usually achieve ~0.55 V open circuit voltages (V_{oc}), 15-25 mA/cm^2 short circuit current densities (J_{sc}), > 55% fill factor (FF), and stable operation over long periods of time [4–6]. The state-of-the-art certified CQD solar cells show an overall power conversion efficiency (PCE) of ~8.5% and these devices are stable in air [7]. This performance is only achieved through fine tuning of the CQD band gap by varying quantum dot sizes as well as incremental improvements in the CQD quality and its ligands. Reduction of bandgap traps through chemical passivation treatments was found to be highly important to achieve high efficiency in CQD solar cells [8]. Although CQD's carrier mobility has been improved steadily over the years and reported values have reached 1-30 cm^2/(Vs), this has not extended the diffusion length anymore due to the still prevalent high recombination center density [9]. Consequently, CQDs devices still have a large mismatch between their charge carrier transport and optical absorption lengths, and only electron-hole pairs generated within the transport length are effectively collected to the electrodes.

In a one-dimensional device this mismatch in characteristic lengths impends a limitation in CQD-based photovoltaic technology [10,11]. However, for a two or three-dimensional structure, this restriction does not play the same role. In fact, without improving upon those lengths, it should be possible to design structures that can trap all the light in the CQD absorption range while still effectively extracting charges. In this paper we present a detailed optoelectronic simulation of TiO$_2$-PbS heterojunctions in flat and grating patterned

microstructures that clearly illustrate the need for balancing the optical absorption length with the charge transport length in order to achieve high performing devices. We demonstrate that the transport length limitation is eliminated through micro-structuring the CQD device with a simple two-dimensional (2D) geometrical periodic pattern. In particular, we simulated a series of patterned 2D PbS solar cells with different parameters and achieved a PCE as high as 11.2% with a J_{sc} of 35.2 mA/cm^2, which shows the great opportunity and potential of photonic microstructure design in CQD solar cells.

2. Theoretical basis

In order to understand the operational electronic mechanisms of quantum dot solar cells and to optimize their design, various computational methods have been applied [12–15]. Among them, numerical simulations based on the drift-diffusion transport are known as the best approach for evaluating generation-recombination processes in the hetero-structured devices [16]. However, for CQD heterojunction solar cells, the complete optical generation and transport processes employing calculations of the optical absorption are rare [17]. We applied a 2D model using the commercial simulation software COMSOL multiphysics based on the finite element method to obtain accurate calculations of both the photonic and electronic characteristics of CQD heterojunction solar cells [16, 18].

The model was constructed in the following way: first, the optical field distribution within the solar cells was simulated to obtain the carrier generation profile utilizing COMSOL radio-frequency module. This module strictly applies Maxwell's equations in a unit cell surrounded by Floquet-Bloch boundaries. A monochromatic plane wave was used as the light illumination, while the input sun energy was swept from 350 nm to 1160 nm to recreate the cell spectral response in the main absorption region of PbS CQDs. The input power of each wavelength was set to a value corresponding to the AM 1.5G solar reference spectrum. All the materials' optical properties were utilized without approximations to include absorption and dispersion, and can be found in the Appendix.

A seamless connection within the software transferred the generation distribution obtained from the optical calculation to the electronic modules where the electric potential, charge carrier transport, recombination, and collection processes were comprehensively calculated. In particular, for the recombination term we employed the classic Shockley-Read-Hall expression which explicitly accounted for a trap density. In this model excess carriers recombined by interacting through those intermediate centers. The electrical contacts that constituted the upper and lower boundary of the device were considered as ideal ohmic contacts, which meant that the carrier concentrations were at their thermal equilibrium values at these points. In the end, in order to obtain an accurate carrier concentration, the size of the meshes in the electrical modules was only one-tenth of that in the optical module. All details regarding the simulation implementation can be found in the Appendix.

3. Results and discussion

The solar cells were modeled in a conventional architecture with layers of ITO/TiO$_2$/PbS/MoO$_3$/Ag on a glass substrate (Fig. 1(a)). For the flat "control" devices, the ITO and TiO$_2$ layers were 90 nm and 10 nm thick respectively, while the thicknesses of the top electrode layers, MoO$_3$ and Ag, were 10 nm and 60 nm, respectively. The electronic parameters of PbS and TiO$_2$ which constitute the p-n junction are listed in Table 1, and were obtained from recent literature sources [4, 5, 9,19].

A series of simulations were performed with different PbS thicknesses while keeping all of the other parameters unchanged. A thick PbS layer is expected to absorb more light; however charge carriers are susceptible to recombine if their transit time exceeds the charge recombination lifetime. As a result, the optimized flat structure must balance the two competing processes [10]. The absorption spectra of PbS layers in the devices with 340 nm and 600 nm PbS films are shown in Fig. 1(b). Although the 600 nm PbS device absorbs much more light than the 340 nm one; the J_{sc} of the 600 nm PbS device is significantly lower, and the open circuit voltages (V_{oc}) decreased slightly as well (Fig. 1(c)). Figures 1(d) and 1(e)

show the values of the J_{sc} and PCE as a function of PbS thickness, and those of V_{oc} and FF, respectively. The J_{sc}, $V_{oc,}$ and PCE all increase with the PbS thickness and reach the highest values at 340 nm, but begin to decrease for the thicker films. Consequently, optimized flat solar cells are capable of generating a maximum photocurrent density of about 21 mA/cm^2, which agrees well with current experimental reports [4]. This performance limit originates from the absorption-extraction compromise, wherein the photon absorption length in the infrared exceeds the transport length by about a factor of ~10. In the active layer, the carrier pairs can be generated in both the depletion and quasi-neutral regions. The electron-hole pairs generated in the depletion region can be separated by the electrostatic field. The electron-hole pairs photo-generated within the quasi-neutral portion of the active layer must diffuse to the depletion region to be efficiently separated and extracted [11]. The diffusion length, L_D, of charge carriers is related to the square root of the mobility-lifetime product, $\mu\tau$, according to [10]

$$L_D = \sqrt{\frac{K_B T}{q} \mu\tau}.$$

where μ is the carrier diffusion coefficient, τ is the carrier life time, q is the electronic charge, K_B is the Boltzmann's constant, and $T = 300\ K$ is the operating temperature. In a CQD solid state film with a high trap state density, where the radiative recombination rate is much smaller than trap-related recombination rate, the overall life time reduces to the trapping lifetime, and is inversely proportional to the mobility, rendering L_D mobility invariant [9]. Today's experimentally observed trap state density is at a level of 10^{16} cm^{-3}, and thus the diffusion length is no greater than 100 nm [9]. The depletion region of p-type PbS and high n-type TiO$_2$ heterojunction is about 200 nm [4] (becoming even less for lower TiO$_2$ doping). This explains why the J_{sc} increases slightly and then drops when the active layer is beyond 300 nm. Besides, at the maximum power point (M_{pp}), the depletion region in the PbS active layer is even shorter, as shown in Fig. 2(a), and the collection of the photocarriers relies more heavily on the diffusion process. Figure 2(b) shows that the electric field at M_{pp} drops slightly when the PbS thickness is increased, deteriorating further the charge collection efficiency, so thicker devices tend to give rise to low fill factors which are experimentally observed (See Fig. 1(e)).

Table 1. Parameters employed in simulations of PbS solar cells.

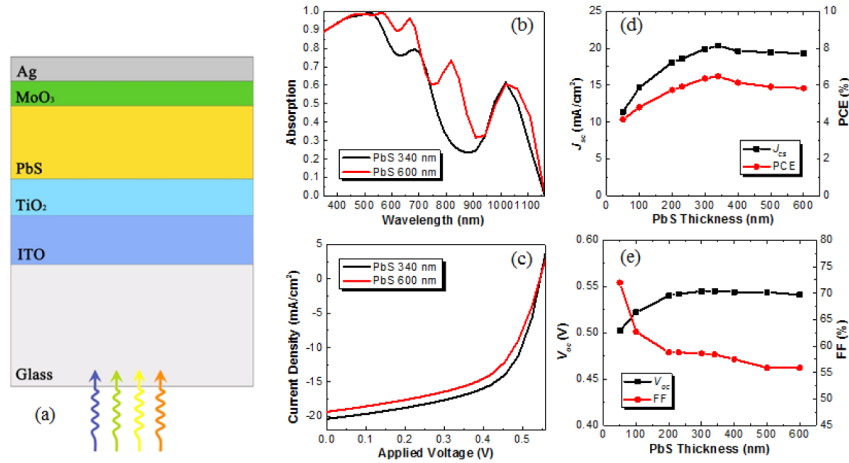|	PbS	TiO$_2$
Doping (1/cm^3)	10^{16} [4]	5×10^{17} [4]
Band-gap (eV)	1.3 [5]	2.4 [5]
Affinity (V)	3.8 [5]	4.1 [5]
Electron Mobility (cm^2/(Vs))	10^{-2} [9]	1 [19]
Hole Mobility (cm^2/(Vs))	10^{-2} [9]	1 [19]
Electron Lifetime (s)	2×10^{-7} [9]	10^{-5} [19]
Hole Lifetime (s)	2×10^{-7} [9]	10^{-5} [19]

Fig. 1. Simulation results in flat PbS solar cells: (a) The schematic diagram of the flat solar cells. (b) The absorption spectra of PbS layers in the flat devices with 340 nm and 600 nm PbS films. (c) J-V curves of 340 nm and 600 nm PbS solar cell devices. (d) J_{sc} and PCE, (e) V_{oc} and FF as a function of PbS thickness.
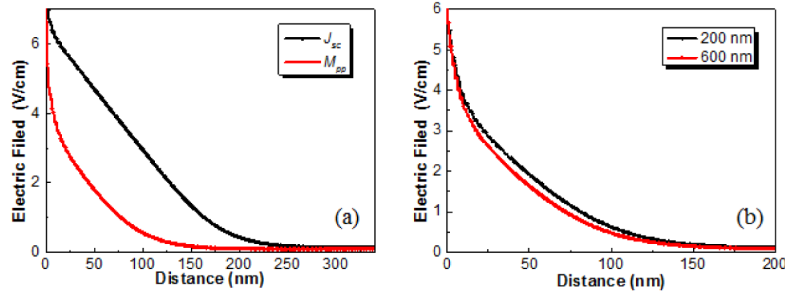

Fig. 2. (a) Simulated electric field intensity as a function of position within the PbS layer at the short-circuit condition and M_{pp} condition. (b) Electric field at the M_{pp} condition in the flat devices with 200 nm and 600 nm PbS films.

A path to overcome this limit, without expecting material improvements, is to go beyond 1D flat device. This approach is in principle quite simple, the rational for the design is to recognize the limits imposed by the transport length and create a cell structure that is able to capture more light without upsetting the electronic performance. A grating structure, where the flat film is ideally wrapped around in a conformal fashion is the simplest way to numerically test this idea. In essence this means packing more absorbing material per unit of effective cross area without upsetting the transport length limit. Figure 3(a) shows a unit cell of such a grating solar cell. On top of a glass substrate, a first flat ITO layer is layered for bottom contact. The grating is then defined by a transparent periodic optical dielectric covered by a second ITO coating. The core of the grating could be made of any transparent material as the second ITO layer gives a path for the carriers. However, we found that its index of refraction plays a significant role enhancing light trapping. In the rests of the simulations we used TiO_2 because its high index and low absorption favored light absorption in the PbS layer. The total thickness of the two ITO layers is always > 90 nm where they meet, which corresponds to the thickness of the ITO of the flat solar cells. The subsequent layers are coated onto the ITO-TiO_2 grating in the same sequence as in the flat one. We set the first ITO layer, MoO_3, and metal contact thicknesses to the same values used in the flat devices, while allowing for optimization on the PbS thickness, grating height and pitch, as

well as the thickness of the electronically active TiO_2 and second layered ITO (the optimized geometry values are summarized in the Appendix).

The effect of the grating height is shown in Figs. 3 and 4 with all the other parameters set to the optimized values. The absorption spectra of the PbS layer and that of the whole device with 2 μm grating height is shown in Fig. 3(b). The active layer of this device can absorb more than 90% of the light in the visible and retain above 80% up to the end of the infrared absorption. The carrier generation rates per unit area as a function of the effective PbS thickness in both the flat and patterned PbS solar cells are shown in Fig. 3(c). The patterned device achieves more photo-generated carriers than the flat one of the same PbS volume, which is the result of high localization of the optical field in the grating structure. In Figs. 3(d) and 3(e), the absorption in the two types of devices –with grating and flat, both of 388 nm effective PbS thickness – is clearly shown with strong absorption being present in the grooves of the grating.
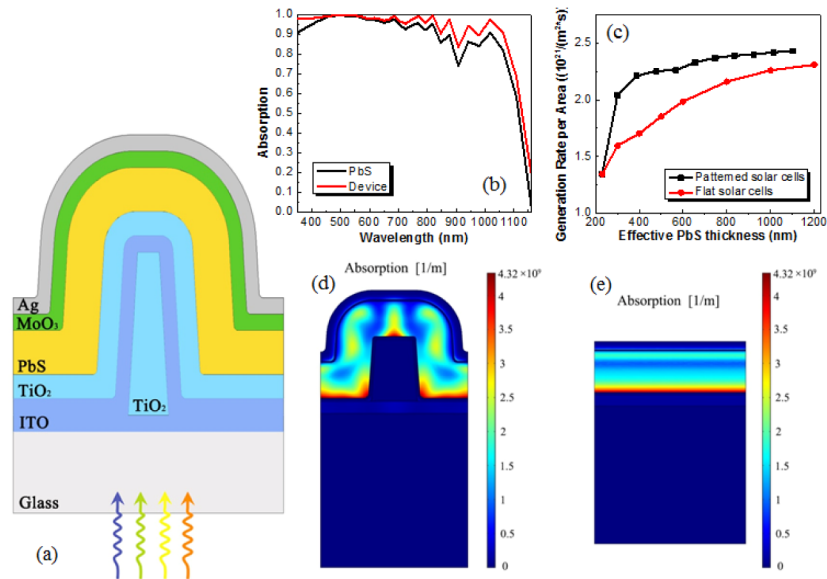

Fig. 3. (a) The schematic diagram of the patterned solar cells. (b) The absorption spectra of the PbS layer and that of the whole device with 2 ¦Ìm grating height. (c) Generation rate per unit area as a function of effective PbS thickness in patterned and flat devices. (d) and (e) Optical absorption in patterned and flat devices with 388 nm effective thickness.

The J-V curve of the 2 μm high grating device and the J_{sc} as a function of grating height are shown in Figs. 4(a) and 4(b), respectively. Here the volume of PbS is increased just by increasing the grating heights, keeping the PbS film thickness automatically always within the transport length. We can notice that the J_{sc} continues increasing with the grating height until it is saturated at about 35.2 mA/cm^2. Comparing to the flat devices, the J_{sc} in patterned structures increased by about 15 mA/cm^2. Given that an AM 1.5 solar flux would translate to 40 mA/cm^2 for a 100% efficient photon-to-electron conversion in PbS, this model predicts an overall 88% photon-to-electron conversion efficiency at J_{sc}, comparable to what is practical in more established materials with similar optical absorption range such as standard silicon or CZTSSe cells [20, 21]. Figure 4(b) also shows that the PCE follows the J_{sc} improvements with the grating height, reaching a peak value of 11.2%. The simulation also indicates that although the FF in the shorter grating is lower than that of flat devices, it continues improving slightly with grating heights, as shown in Fig. 4(c). This result is somewhat counterintuitive, however since the PbS layer maintains the same thickness, the electric field does not decrease when the grating height is increased (Figs. 4(d) and 4(e) show the 2D electric field intensity in the grating devices with 400 nm and 2000 nm heights). In fact, with larger grating heights,

there is a stronger light absorption localization on the top and bottom of the grating near the heterojunction interface, heightening the electric field intensity and hence the FF slightly. In fact, if the PbS thickness increases perpendicular to the heterojunction interface, the absorption-extraction compromise is optimized at a thickness of 230 nm (as shown in Fig. 5), that is smaller than the thickness of the optimized flat cell, which confirms that the benefits of the patterned structure can only be achieved by keeping the PbS thickness within the transport length.
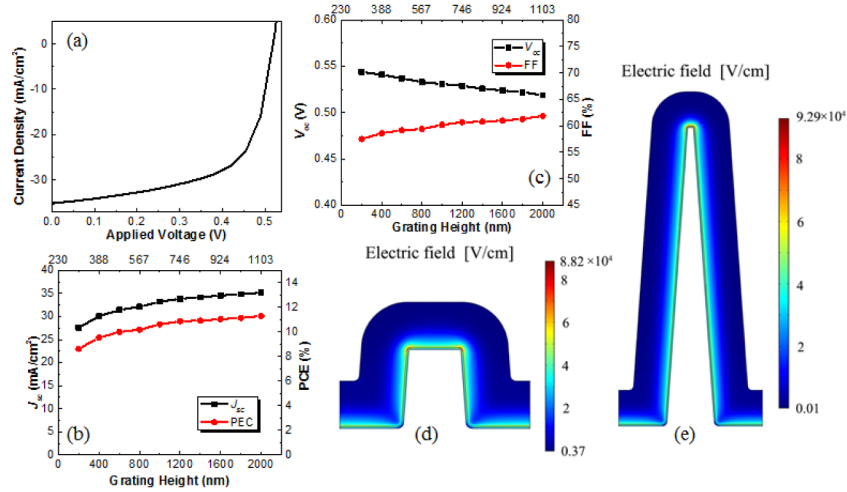
Fig. 4. Simulation results in grating PbS solar cells: (a) J-V curve of a 2 μm high grating PbS solar cell device. (b) J_{sc} and PCE, (c) V_{oc} and FF as a function of grating height. (c) and (d) Electric field at the M_{pp} condition in the patterned devices with 400 nm and 2000 nm heights. Notice slightly larger numbers for the scale in the grating structure.
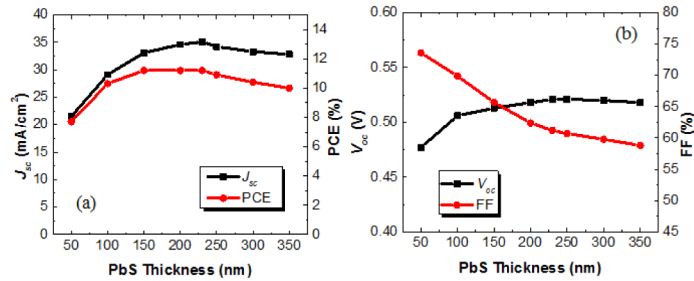

Fig. 5. Plots of (a) J_{sc} and PCE, (b) V_{oc} and FF as a function of PbS thickness in grating PbS solar cells.

The n-type material of the heterojunction, TiO$_2$, plays an important role in the device properties. Figure 6(a) shows the J_{sc} and PCE both decreasing somewhat with increasing TiO$_2$ thickness. A thinner TiO$_2$ layer forces more of the electrostatic field into the PbS layer, helping the carrier pairs to be separated and extracted more efficiently. Therefore, a 10 nm TiO$_2$ layer was used in the optimized patterned solar cell device. ITO is commonly used in solar cell devices as a transparent electrode, but it has high absorption in the infrared wavelength region. In Fig. 6(b), the J_{sc} and PCE as a function of the patterned ITO thicknesses are plotted (the bottom flat ITO thickness was left constant to 80 nm). Because more light is absorbed in ITO layer instead of the PbS layer, a thicker ITO layer leads to lower J_{sc} in general, with a little bump in the downward trend around 70 nm due to optical redistribution. A 10 nm patterned ITO layer together with the 80 nm ITO layer underneath is considered to provide a good balance between electrical conductivity and transparency.

Different grating periods were also calculated with the results shown in Fig. 6(c). The effective PbS thickness decreases with the grating interval, but the optical distribution also changes resulting in a slight decline of current after the pitch goes above 1150 nm. This decline is not abrupt, giving space to accommodate the grating wall coatings with increase easiness without losing much of the photocurrent density. The 960 nm pitch gives the highest PCE and it was subsequently chosen to be used in the optimized device. Shorter pitches were not considered as the coated walls would be impossible to accommodate.
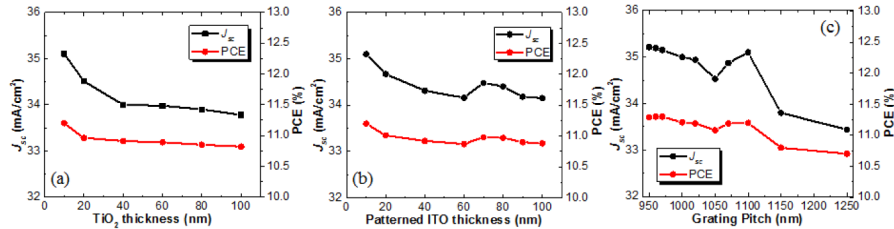

Fig. 6. Plots of J_{sc} and PCE as a function of (a) TiO_2 thickness, (b) patterned ITO thickness, and (c) grating pitch.

The present results indicate that in general this simple design is robust to small geometrical variations and we could consider its fabrication. A periodic grating structure with ~1 μm pitch could be built by a large variety of scalable low cost methods, such as nanoimprint lithography of TiO_2 nanoparticle paste or large scale interference lithography of a mask polymer, followed a physical evaporation method such as sputtering. The grating aspect ratio is not too large and it could allow for quasi-conformal deposition of the required subsequent layers using conventional evaporation methods for most of the oxides and metallic layers, while dip-coating could be employed to create a uniform CQD layer on the patterned structure [6]. We restricted our work to a 2D structure but it is likely that a 3D arrangement would make nanofabrication somewhat easier because the height of structures could be lowered as more PbS mass could be packed per unit area and still respect the transport limits. In this paper, we did not prove that in particular but nevertheless successful nanofabrication of 3D structures with the complexity and scale of the ones proposed here has been experimentally demonstrated in other solar cell materials [22]. Nevertheless, in general for patterned devices it is a challenge to avoid additional nanofabrication defects. However this is a technological challenge and not an intrinsic problem. As this works illustrates, utilizing strictly the same physical parameters, a change in geometry could open a door to improved performance for transport limited materials. Recent publications with patterned CQD PbS cells have shown this is indeed possible [17, 23]. Researchers have demonstrated enhancement in photocurrent with modest losses in FF and V_{oc} for patterns involving micron-size pyramids and nanosphere templated gratings.

4. Conclusion

In conclusion, a 2D model based on the finite element method has been developed to simulate the full optoelectronic characteristics of 1D and 2D TiO_2-PbS CQD heterojunction solar cells. The electrical characteristics of the solar cells have been calculated in the patterned PbS solar cells with different geometric parameters. Our optimized device significantly increased the solar cell PCE to 11.2%, with a J_{sc} of 35.2 mA/cm^2, exceeding the previous limits of the carrier diffusion length in these devices. The geometry of the patterned device is simple and with proper large-area conventional microfabrication procedures and tools, it could be realized to heighten the efficiency of CQD solar cells.

Appendix

The model was constructed in the following way: first, the optical field distribution within the solar cells was simulated to obtain the carrier generation profile utilizing COMSOL radio-frequency module. This module strictly applies Maxwell's equations on a unit cell surrounded by Floquet-Bloch boundaries. A monochromatic plane wave was used as the light input, while the input sun energy was swept from 350 nm to 1160 nm to recreate the cell spectral response in the main absorption region of PbS CQDs. The input power of each wavelength was set to a value corresponding to the AM 1.5G solar reference spectrum. The local wavelength-dependent generation could then be expressed as

$$g(x, y, \lambda) = -\alpha P(x, y, \lambda) \lambda / hc, \tag{2}$$

where $P(x, y, \lambda)$ is the light intensity within the active layer volume as a function of position (x,y), λ is the wavelength, h is the Plank's constant, c is the speed of light in vacuum, $\alpha = 4\pi\kappa / \lambda$ is the absorption coefficient, and κ is the imaginary part of the frequency dependent complex refractive index. Thus, the total generation rate distribution G is the integration of $g(x, y, \lambda)$ on λ over the spectral band of the absorption.

A seamless connection within the software transferred the generation distribution G obtained from the optical calculation to the electronic modules where the electric potential, charge carrier transport, recombination, and collection processes were comprehensively calculated. The electrostatic potential (Φ) was calculated by solving the Poisson's equation:

$$\nabla^2 \Phi = \frac{q}{\varepsilon_0 \varepsilon_r}(n - p - N). \tag{3}$$

Here n and p are the electron and hole concentrations, respectively, and the impurity concentration, $N \equiv N_d - N_a$, is defined as the sum of the concentrations of ionized donors N_d and the acceptors N_a. The electron and hole concentrations were calculated in two convection-diffusion modules based on the equations displayed below under the effects of carrier diffusion, drift, generation and recombination.

$$\nabla[-D_n \nabla n + n\mu_n(\nabla\Phi + \frac{\nabla\chi}{q} + \frac{K_B T}{q}\nabla \ln N_c)] = G(x, y) - R, \tag{4}$$

$$\nabla[-D_p \nabla p - p\mu_p(\nabla\Phi + \frac{\nabla\chi}{q} + \frac{\nabla E_g}{q} - \frac{K_B T}{q}\nabla \ln N_v)] = G(x, y) - R, \tag{5}$$

where $D_n = \mu_n K_B T / q$ ($D_p = \mu_p K_B T / q$), is the electron (hole) diffusion coefficient, μ_n (μ_p) is the electron (hole) mobility, q is the electronic charge, χ is the electron affinity, E_g is the semiconductor band gap, K_B is the Boltzmann's constant, $T = 300\ K$ is the operating temperature, G is the carrier generation rate calculated in the optical module as described above, and R is the carrier recombination rate. $N_c = [m_c K_B T / (2\pi\hbar^2)]^{3/2}$ ($N_v = [m_v K_B T / (2\pi\hbar^2)^{1/2}]$) is the effective conduction (valence) band density of states, where m_c (m_v) is the conduction (valence) band effective mass, $\hbar$ is the reduced Plank's constant, g is the carrier generation rate. At low-to-moderate carrier concentrations, the Shockley-Read-

Hall recombination dominates, in which excess carriers recombine by interacting through intermediate centers. The recombination term R was give as,

$$R_{srh} = \frac{np - n_i^2}{\tau_n(p + p_t) + \tau_p(n + n_t)},$$ (6)

where τ_n (τ_p) is the electron (hole) life time, n_t (p_t) is the electron (hole) concentration of the trap state, $n_i = [N_c N_v \exp(-qE_g / K_B T)]^{1/2}$ is the intrinsic carrier concentration, and the largest Shockley-Read-Hall recombination happens when $n_t = p_t = n_i$.

In the electronic modules, it was very important to set good initial solution guesses of the potential to get accurate final simulation results. The initial potential was set based on the following analytical expression for the built-in voltage in a n-p heterojunction,

$$\Phi_0 = \chi_2 - \chi_1 + \frac{1}{q}[E_{g2} - K_B T \ln(\frac{N_{c1} N_{v2}}{N_d N_a})],$$ (7)

where χ_1 (χ_2) is the affinity of n (p) type semiconductor, here TiO$_2$ (PbS), N_d (N_a) is the doping concentration of the n (p) type semiconductor, and N_{c1} (N_{v2}) is the effective conduction (valence) band density of states of n (p) type material. Considering the interface of the heterojunction as the potential reference, the initial potentials at the ends were obtained from the potential drop at each side,

$$\Phi_n = \Phi_0 \frac{\varepsilon_p N_a}{\varepsilon_p N_a + \varepsilon_n N_d},$$ (8)

$$\Phi_p = -\Phi_0 \frac{\varepsilon_n N_d}{\varepsilon_n N_d + \varepsilon_p N_a},$$ (9)

where ε_n (ε_p) is the permittivity of the n (p) type material. The thermal-equilibrium majority carrier concentration in n and p type semiconductors could be written as

$$n_0 = N_d \exp[\frac{q(\Phi - \Phi_n)}{K_B T}],$$ (10)

$$p_0 = N_a \exp[\frac{-q(\Phi - \Phi_p)}{K_B T}].$$ (11)

Then the minority carrier concentration could be obtained according to the carrier concentration relationship at the thermal equilibrium

$$np = n_i^2.$$ (12)

Employing Φ_n and Φ_p as the initial value and considering the relationship between carrier concentration and potential, the equilibrium potential at zero applied voltage and without illumination could be solved in an independent electrostatic module. After that, the non-equilibrium potential and carrier concentrations at different applied voltage (V_d) with 1 sun light illumination were calculated in another electrostatic module and two convection-diffusion modules. These three modules coupled together through sharing the variables Φ, p, and n were solved by a COMSOL direct solver.

The electrical contacts that constituted the upper and lower boundary of the device were considered as ideal ohmic contacts, which meant that the carrier concentrations were at their thermal equilibrium values n_{int}, p_{int} at these points. According to the neutral charge condition, they obeyed the following expression,

$$n_{init} - p_{init} - N = 0. \tag{13}$$

Considering Eq. (11), the thermal equilibrium carrier concentrations at the boundaries were solved to be

$$p_{init} = \sqrt{n_i^2 + N^2/4} - N/2, \tag{14}$$

$$n_{init} = \sqrt{n_i^2 + N^2/4} + N/2. \tag{15}$$

For Poisson's equation under an external electric bias (V_d), it was assumed that the potential Φ at the anode end was unchanged, while at the cathode end was decreased by V_d from its initial value, where V_d was swept from 0 V to 1 V. Finally, the conservative form of the convection-diffusion equations, with ideal weak constraints and quadratic Lagrange elements was used to obtain the current at the surface of the solar cells. For the heterojunction device simulated in this paper, zero charge and no flux conditions were used in the transverse direction for the electrostatic potential and carrier diffusion modules, respectively. In the end, in order to obtain an accurate carrier concentration, the size of the meshes in the electrical modules was only one-fifth of that in the optical module. Optimized Geometry Parameters of Patterned PbS solar cells are shown in Table 2. To optimize the PbS, and TiO2, patterned PbS thicknesses, the grating pitch was set to 1100 nm, to open big enough intervals for all the layers, with the other parameters the same as in the table. For optimization of pitch and height, the thicknesses of the layers were set exactly the same as in the table. The same thicknesses are also used in the flat devices.

Table 2. Optimized Geometry Parameters of Patterned PbS solar cells (nm).

Pitch	960
Flat ITO	80
Patterned ITO	10
TiO$_2$	10
PbS	230
MoO$_3$	10
Ag	60
Height	2000

All the materials' optical properties were utilized without approximations to include absorption an dispersion, as shown in Fig. 7. The depletion region in the p-type PbS decreases with TiO2 doping as shown in Fig. 8. Figure 9 shows the absorption spectra in PbS layers of the patterned devices with different materials in the core of the grating. While ITO absorbs light and air causes high localization in it, TiO2 with a high index and low absorption makes PbS layer absorb the most light. The PbS layers in both the flat and patterned solar cell devices absorbed most of the light as shown in Fig. 10.
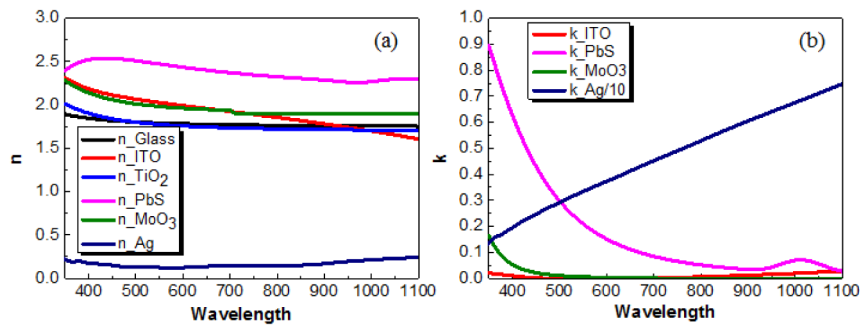

Fig. 7. (a) Real and (b) imaginary parts of the refractive index of each layer in the solar cell device. The imaginary parts of TiO$_2$ and glass indexes are too low to be shown here, and can be considered transparent.
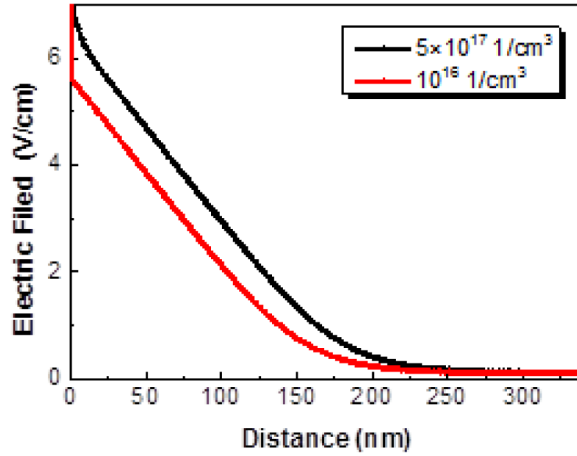
Fig. 8. Simulated electric field intensity as a function of position within the PbS layer at the short-circuit condition in the devices with different n-type doping TiO_2.
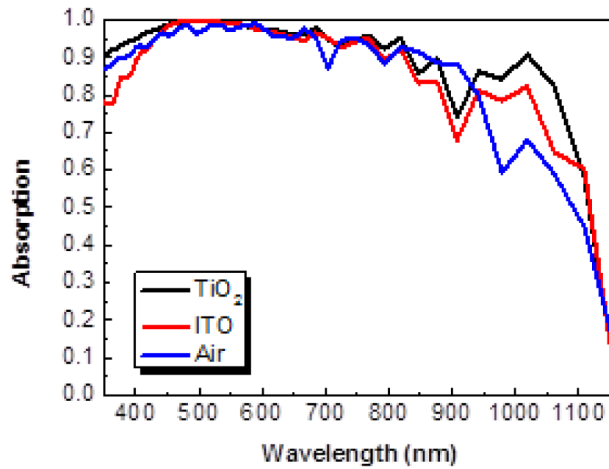

Fig. 9. Absorption in PbS layers of the patterned devices with different materials in the core of the grating.
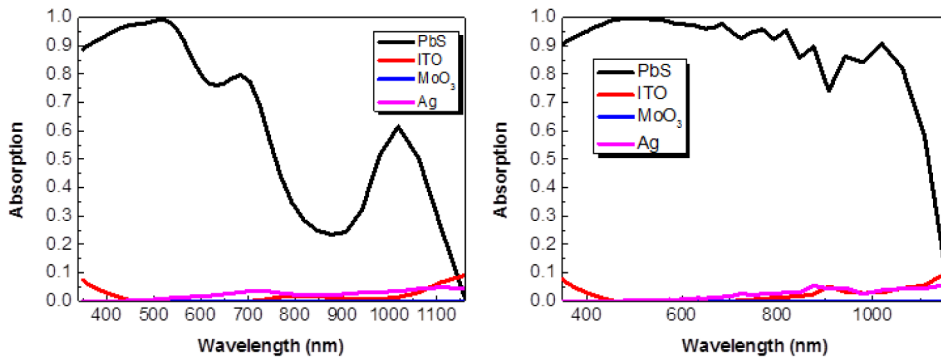

Fig. 10. Absorption in different layers of the (a) flat and (b) patterned devices.